IEEE Access
Multidisciplinary ⋮ Rapid Review ⋮ Open Access Journal

Received 5 December 2023, accepted 25 December 2023, date of publication 15 January 2024, date of current version 31 January 2024.

Digital Object Identifier 10.1109/ACCESS.2024.3354375

APPLIED RESEARCH

Analysis of Design Requirements and Optimization Possibilities of Partial Power Converter for Photovoltaic String Applications in DC Microgrids

ANDRII CHUB, (Senior Member, IEEE), NASER HASSANPOUR, (Student Member, IEEE), NEELESH YADAV, (Member, IEEE), TANEL JALAKAS, (Member, IEEE), ANDREI BLINOV, (Senior Member, IEEE), AND DMITRI VINNIKOV, (Fellow, IEEE)
Department of Electrical Power Engineering and Mechatronics, Tallinn University of Technology, 19086 Tallinn, Estonia

Corresponding author: Andrii Chub (andrii.chub@taltech.ee)

This work was supported in part by the Estonian Research Council under Grant PRG1086; and in part by the Estonian Centre of Excellence in Energy Efficiency, ENER, funded by the Estonian Ministry of Education and Research under Grant TK230.

ABSTRACT The paper analyzes the application flexibility of partial power converters for interfacing photovoltaic strings in dc microgrids. Step-up/down partial power converters were considered for providing the lowest active power processing. This study considers three Si-based photovoltaic modules commonly used in residential applications: 54-, 60-, and 66-cell. Different configurations of photovoltaic strings are analyzed to find at what voltages most energy is generated in hot and cold climates. Combining these results with the operating voltage range of a droop-controlled dc microgrid yields design requirements for the partial power interface converters. The proposed design limits the maximum power the converter processes to optimize its components. Next, the application of the topology morphing control is studied regarding the performance enhancement of partial power converters. Experimental results verify good converter performance and feasibility of efficiency improvement with the topology morphing control.

INDEX TERMS DC-DC converters, dc microgrids, partial power conversion, photovoltaic energy.

I. INTRODUCTION

Power electronic converters are the backbone of future energy use, considering the increasing electrification of technical processes [1], [2], [3]. The deployment of renewable energy sources keeps growing year-to-year, pushing the power electronics industry to produce converters with better performance and lower cost [4], [5]. Despite its intermittent nature, photovoltaic (PV) energy is considered the most promising solution for a sustainable future [6]. The cumulative PV generation capacity has recently reached 1 TW [7]. All these developments pushed the technology of power converters for large-scale PV installations to a good level of maturity [8], [9].

The associate editor coordinating the review of this manuscript and approving it for publication was Nagesh Prabhu.

At the same time, PV technologies enable nearly zero-energy buildings by replacing electricity demand with on-site energy generation [10], [11]. PV string inverters are also widely available and highly efficient [12]. The next step in the efficiency enhancement of residential and small commercial buildings is the adoption of dc microgrids [13], [14], [15]. However, dc-dc power electronics converters for these applications are based on the conventional full power processing approach, which is mature and limited by the barriers of the existing technologies of semiconductor and passive components [16].

Partial power processing is a novel concept for dc-dc energy conversion, as shown in Fig. 1. It allows for processing only a fraction of the total power, reducing the power losses to much below those of conventional full-power converters [17]. Partial power converters (PPCs) are typically implemented

using an isolated dc-dc cell that is connected in parallel to one of the ports (V_{DC} in Fig. 1) and in series between the ports on the other side (V_C in Fig. 1) [16]. The dc-dc cell regulates the voltage difference between two ports, i.e., the voltage of the series-connected side (V_C in Fig. 1). As a result, the parallel high-voltage (HV) port is rated for full voltage but partial current. Also, the series low-voltage (LV) port operates at full current and partial voltage. The power processed by the dc-dc cell depends on the voltage range in the series port [17]. Hence, PPCs are a niche technology that works best when this voltage range can be narrowed down [18]. It has been demonstrated for PV applications, electric vehicle charging, power flow control in dc microgrids, wind turbines, fuel cells, and other applications [17].

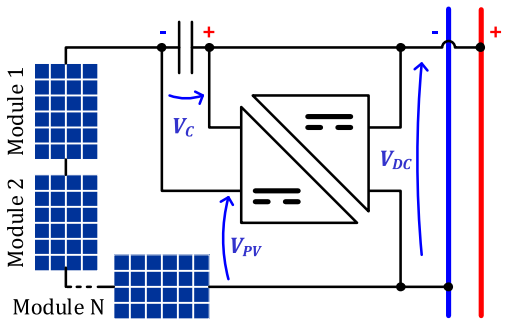

FIGURE 1. The concept of partial power interface converter for integration of PV strings in dc microgrids.

The advantages of PPC technology have attracted the interest of researchers, especially in PV applications [19], [20]. Numerous PPC topologies are proposed for PV string applications [17]. However, only a few show a peak efficiency of at least 99% [16]. Typically, a PPC comprises a voltage-fed dc-dc cell connected in parallel input series output (PISO) configuration and performs either voltage step-up or step-down between two ports [16]. Series input parallel output (SIPO) configurations were also demonstrated recently. It could be concluded from the recent literature that SIPO configuration must be implemented with a current-fed dc-dc to provide a peak efficiency of over 99% [21], [22].

It was shown that the performance of a PPC interfacing a PV string could be improved by limiting the relative amount of power processed by the dc-dc cell, i.e., limiting its partiality coefficient K_{pr} [18]. The concept of step-up/down PPC capable of reversing polarity in the series port voltage (V_C) was introduced to reduce the fraction of the processed power [23], [24]. The step-up/down PPCs can operate with up to two times lower active power than the step-up and -down PPCs in the same applications. Hence, more research is required to establish the most suitable application scenarios and demonstrate performance enhancement techniques.

Prior studies have not targeted PPC applications for interfacing PV strings in droop-controlled dc microgrids, which creates a knowledge gap in this field. In these applications, the voltage of both PV and dc microgrid ports feature some operating range, extending the voltage range in the series port of PPC. For example, the study [23] considered possible variations of the maximum power point (MPP) voltage for hot environmental conditions in Brazil. In contrast, this work considers how MPP voltage varies in hot and cold environmental conditions to show a realistic estimate of possible operating voltage on the PV side, which was not analyzed before. Moreover, it considers three typical residential Si-based PV module types and their different number in a PV string. In addition, the droop control voltage range on the dc microgrid side is included in the analysis. As a result, this study synthesizes practical PPC design requirements for PV string applications in residential dc microgrids, closing the existing knowledge gap in this field. Since voltage variations at both PV string and dc microgrid ports are considered, such an interface step-up/down PPC should operate in a relatively wide dc gain range, which would deteriorate its peak efficiency [18]. Hence, this study also analyzes the feasibility of efficiency improvement by applying topology morphing control (TMC) techniques [25].

Residential droop-controlled dc microgrids with a nominal voltage of 350 V and droop control range of ±30 V are being standardized in the EU [26]. This study analyzes step-up/down PPC technology to provide optimized solutions for integrating PV strings in 350 V residential droop-controlled dc microgrids. This paper builds upon the results published in [27]. The contributions of this paper are as follows:

- Modeling of dependence between energy production and operating voltage for three typical residential PV modules for two climates to define the applicability of step-up/down PPCs for residential PV string.
- Analysis of PPC application requirements and feasibility of PPC-based residential PV string implementations with restricted voltage regulation range, considering the droop control voltage range of residential dc microgrids.
- Demonstration of TMC for efficiency improvement of step-up/down PPCs and experimental performance evaluation of two feasible TMC implementations.

Hence, the paper provides a comprehensive analysis of realistic PPC operating conditions and draws design requirements in Section II. Also, it studies the feasibility of improving PPC efficiency by applying the TMC modulations proposed in Section III. Experimental results in Section IV yield a discussion about the validity of the taken assumptions. The conclusions are drawn in Section V.

II. ANALYSIS OF DESIGN REQUIREMENTS

This section considers three typical PV modules of monocrystalline Si marketed for residential users. Their types and parameters are listed in Table 1. These modules differ in the equivalent number of PV cells, which could also be composed of half-cut cells to reduce in-module conduction losses. As these PV modules have virtually the same surface area, the difference in the number of equivalent cells originates from the use of different standardized sizes of PV cells available on

TABLE 1. Datasheet parameters of residential PV modules.

Parameter	PV modules		
	Qcell Q.PEAK DUO BLK M-G11 [28]	Trina Solar TSM-DE06X.05(II) [29]	Canadian Solar HiKuBlack CS3L-370MS [30]
No. of cells (half cells)	54	66 (132)	60 (120)
Nameplate power, W	400	380	370
$V_{MPP(STC)}$, V	31.2	37.8	34.1
$I_{MPP(STC)}$, A	12.8	10.1	10.9
$V_{OC(STC)}$, V	37.2	45.5	40.8
$I_{SC(STC)}$, A	13.4	10.5	11.5
$V_{MPP(NOCT)}$, V	29.7	35.6	31.9
$I_{MPP(NOCT)}$, A	10.1	8.1	8.7
$V_{OC(NOCT)}$, V	35.1	42.8	38.5
$I_{SC(NOCT)}$, A	10.8	8.5	9.3
NOCT, °C	42±3	43±2	42±3
β, %/K	-0.27	-0.25	-0.25
γ, %/K	-0.34	-0.34	-0.34

the market [16]. Hence, nearly the same power is achieved at different MPP voltages. This phenomenon allows for making PV strings of different power levels, i.e., suitable for various roof areas, within a limited MPP voltage range.

To identify practical MPP voltage range, modeling of annual energy yield was performed using mission profiles of the solar irradiance and ambient temperature recorded in Arizona, USA, and Aalborg, Denmark. The methodology [31] based on approximating the MPP voltage and current using the Lambert W_0 function was used. This methodology assumes that the PV modules are installed at the optimal angle corresponding to the location latitude to estimate the maximum available PV energy. The modeling is based on fitting some parameters using a specialized add-on of the PSIM software and datasheet parameters for the standard test conditions (STC) and nominal operating cell temperature (NOCT), such as the short-circuit current (I_{SC}), open-circuit voltage (V_{OC}), MPP voltage (V_{MPP}), MPP current (I_{MPP}), V_{OC} temperature coefficient (β), and MPP power temperature coefficient (γ). All other assumptions and modeling constants/coefficients are assumed to be the same as in [31]. The modeling assumes a PV string always operates in the MPP. Twenty eight yearly simulations were performed.

The modeling results are given in Fig. 2, where the height of each bar corresponds to the annual energy generated within a given voltage band. PV strings operate at higher MPP voltages but produce less PV energy in cold climates than in hot ones. Performing analysis for both climate types allows for demonstrating real variability of the MPP tracking range required for each PV string configuration. It was identified that the PV voltage range between 250 V and 450 V can accommodate fourteen possible PV string configurations using the selected three PV module types:

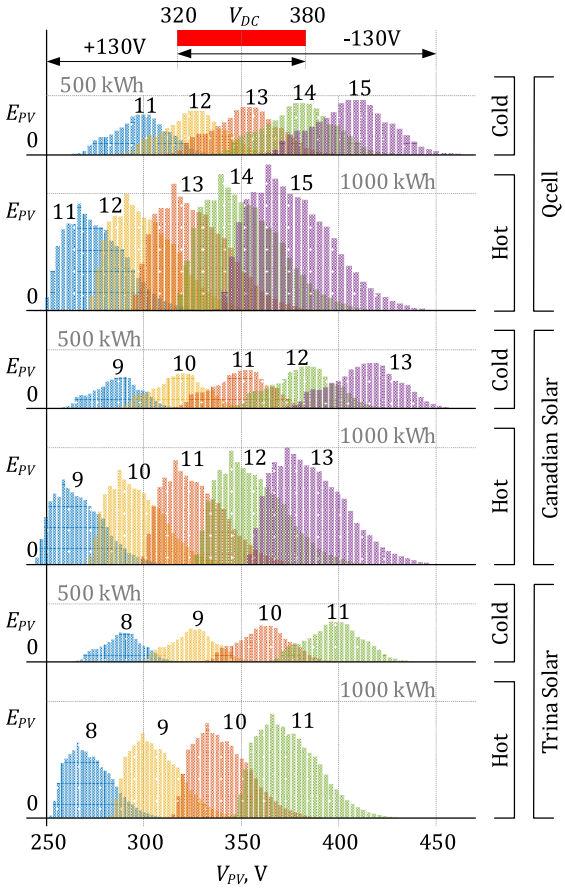

FIGURE 2. Probability of annual PV energy production versus PV string voltage for different PV strings in hot and cold climates for three PV module types.

1) 54-cell PV module: PV strings of 11 to 15 modules are feasible with power ratings between 4.4 kW and 6 kW for the roof installation area between 21 m^2 and 29 m^2.
2) 60-cell PV module: PV strings of 9 to 13 modules are feasible with power ratings between 3.3 kW and 4.8 kW for the roof installation area between 17 m^2 and 24 m^2.
3) 66-cell PV module: PV strings of 8 to 11 modules are feasible with power ratings between 3 kW and 4.2 kW for the roof installation area between 15 m^2 and 21 m^2.

These results prove that PPC technology could be a practical solution for residential PV string applications in dc microgrids. Fig. 2 also depicts the droop-control voltage range of residential dc microgrids between 320 V and 380 V. As a result, an interface step-up/down PPC must be designed for the operating voltage range of the series port voltage V_C of ±130 V. The selected PV string MPP tracking voltage range of 250 V to 450 V limits the PPC power rating at 1.65 kW to cover the selected PV strings with rated power between 3 kW and 6 kW. This variety of power levels and, consequently, the roof surface areas, provide sufficient versatility to suit most small residential installations. Moreover, the PV modules are built in different sizes, simplifying the PV string design for any roof geometry.

The obtained series voltage regulation range of ±130 V should be satisfied even at the lowest dc microgrid voltage of 320 V. This could be converted into the maximum ratio between the dc-dc converter power, i.e., the power processed by PPC, of roughly 40%. However, this metric is misleading as the rated power of dc-dc converter, i.e., the partiality, remains the same for both the maximum and minimum dc microgrid voltages of 320 V and 380 V, respectively. In these points, the dc-dc converter processes up to 1.65 kW, considering the MPP current of the PV modules is below 13 A. Moreover, connecting the parallel port of the PPC to the dc microgrid causes lower worst-case current stress in its semiconductor devices as the dc microgrid voltage range is considerably narrower than the PV string voltage range.

It is worth mentioning that modern TMC techniques employ the capability of some dc-dc converters to reconfigure their topology. Typically dc gain is changed in integer steps to optimize converter operation in a wide input voltage range. The next section presents the case-study PPC topology and demonstrates possible TMC implementation that will be evaluated experimentally.

III. TOPOLOGY AND CONTROL OF THE CASE-STUDY PPC

The topology of the case-study step-up/down PPC shown in Fig. 3 was first presented in [27] and analyzed in [32]. It was synthesized from the current-fed dc-dc converter topology described in [33] and [34]. This section presents three possible modulation techniques that could be used for the TMC implementation. Also, it includes a solid-state circuit breaker (SSCB) for protection and soft-start functionality, which results in extra conduction losses during PPC operation.

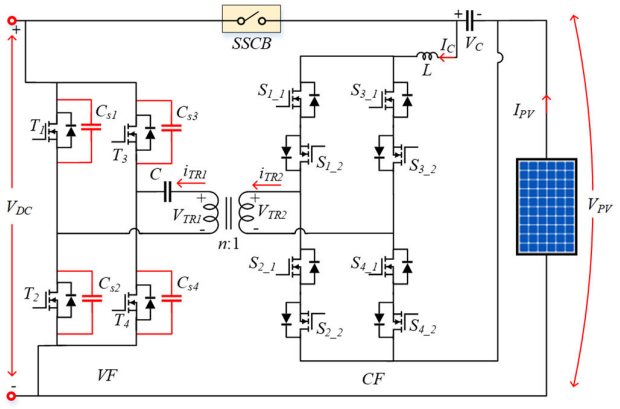

FIGURE 3. Topology and connection configuration of the case-study PPC.

The case-study PPC comprises a dual active bridge dc-dc converter with current-fed (CF) and voltage-fed (VF) sides. The converter operation is described for the CF to VF side power flow. In the power stage, the PV and dc bus voltage ranges are considered equal to 250-450 V and 320-380 V, respectively. The VF consists of a full bridge with a capacitor connected in series with the primary side of the transformer. This capacitor enables reconfiguring the full-bridge VF side into the corresponding half-bridge cell. The CF comprises a full-bridge matrix inverter and a series-connected inductor. Four-quadrant switches enable soft-switching of all semiconductors and simple changing of voltage V_C polarity by flipping gating signals in the CF bridge [33], [34].

A. BASELINE MODULATION

The dc-dc converter operation with the baseline modulation [34] is shown in Fig. 4 (a). The baseline modulation (where I_C is negative and CF side voltage is positive) is shown in Fig. 4 (b) and explained as follows. Using this modulation, the switches S_{1_1}, S_{3_1} and S_{2_1}, S_{4_1} operate in PWM mode with a 180° phase shift. Here, the switches S_{2_1}, S_{4_1} are shifted regarding S_{1_1}, S_{3_1}. The phase shift angle $\phi_{control}$ is the main control variable defining the dc-dc converter gain. Interval t_0- t_1 represents the active state of the converter when the power is transferred from CF to VF side.

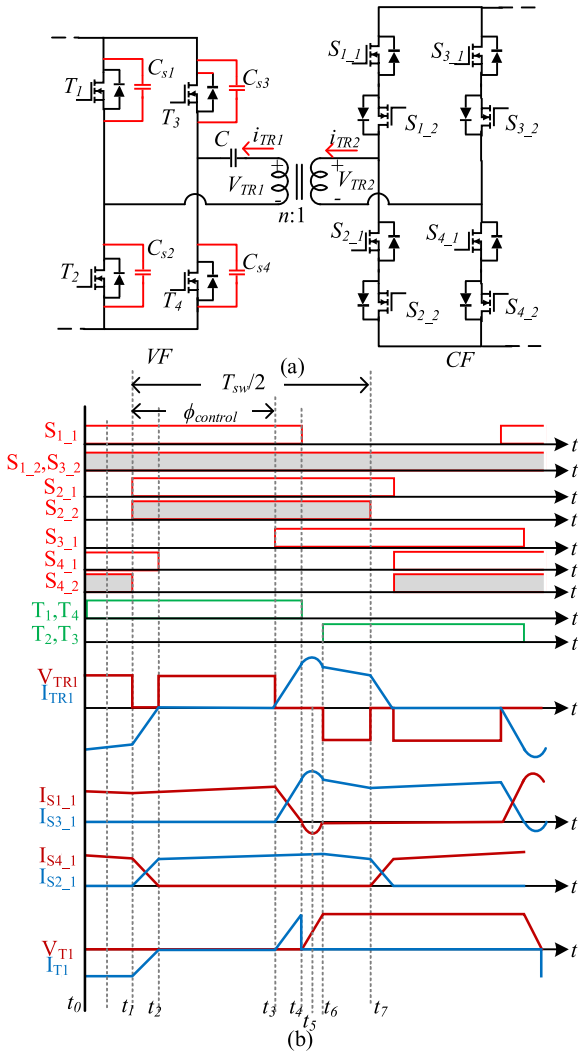

FIGURE 4. Operation of the dc-dc cell with the baseline modulation (a) and the corresponding idealized voltage and current waveforms (b).

During it, the switches T_1 and T_4 are turned on while T_2 and T_3 are turned off. During the interval t_2- t_3, the switches S_{1_1},

S_{1_2}, S_{2_1}, and S_{2_2} conduct to energize the inductor. Turning off of S_{4_1} with ZCS is achieved. In t_4-t_5, the converter current rises with the same slope and exceeds the inductor current.

The current direction reverses in switches S_{1_1} and S_{1_2}, enabling the turning off of switch S_{1_1} with zero-current switching (ZCS). The converter also benefits from ZVS on the VF side. From t_6, the converter enters the next active state and a similar process can be repeated. Soft-switching could be achieved in the same manner for negative CF voltage. It would require the switches S_{2_1}, S_{4_1} to be turned on, while the switches S_{1_2}, S_{3_2} function similarly to a synchronous rectifier. Switches S_{2_2}, S_{4_2} operate with a fixed phase shift with respect to VF side switches and perform the ZVS and ZCS for VF and CF side semiconductors, correspondingly. Equation (1) represents the voltage equation for a PPC, where V_{PV}, V_{DC}, and V_C define the PV voltage, dc microgrid voltage, and the series voltage to the PCC, respectively. A generalized PPC voltage gain (G_{PPC}) can be carried out as (2), where the phase shift angle $\varphi_{control}$ defines the dc gain [33], [34].

$$V_{PV} = V_{DC} + V_C \tag{1}$$

$$G_{PPC} = \frac{V_{DC}}{V_{PV}} = \frac{1}{1 + G_{dc-dc}} \tag{2}$$

Here, the partiality ratio K can be written as (3).

$$K = 1 - \frac{1}{G_{PPC}} \tag{3}$$

The simplified equation for voltage gain of the dc-dc converter G_{dc-dc} can be expressed as (4). The detailed equation of the dc-dc gain is given by (5), where t_{res} represents the resonance period t_4- t_6, and f_{SW} is the switching frequency [33].

$$G_{dc-dc} = \frac{V_C}{V_{DC}} \tag{4}$$

$$G_{dc-dc} = \frac{\pi n}{1 - \frac{\varphi_{control}}{\pi} - 2f_{sw}\left(\frac{2nL(2I_{c(max)} - I_c)}{V_{DC}} + t_{res}\right)}, \tag{5}$$

where $I_{C(max)}$ is the maximum input current of the dc-dc cell defined at the design stage, and I_C is the average input current of the dc-dc cell. This makes the dc gain weakly dependent on the operating power.

B. MODULATION WITH VF-SIDE TMC (TMC-VF)

In the TMC-VF modulation, a small modification is made in the baseline modulation explained earlier. Fig. 5 (a) shows the dc-dc stage operation with the TMC-VF modulation detailed in Fig. 5 (b). The VF side switch T_3 is turned off, and T_4 is turned continuously. At the same time, the switches T_1 and T_2 operate in PWM mode. The CF-side switches are modulated with a duty cycle of slightly over 0.5 to ensure their ZCS and perform synchronous rectification (bottom switches). The time intervals in the switching sequence are essentially the same as in the baseline modulation.

The TMC-VF modulation effectively doubles the normalized dc voltage gain of the dc-dc converter from equation (5),

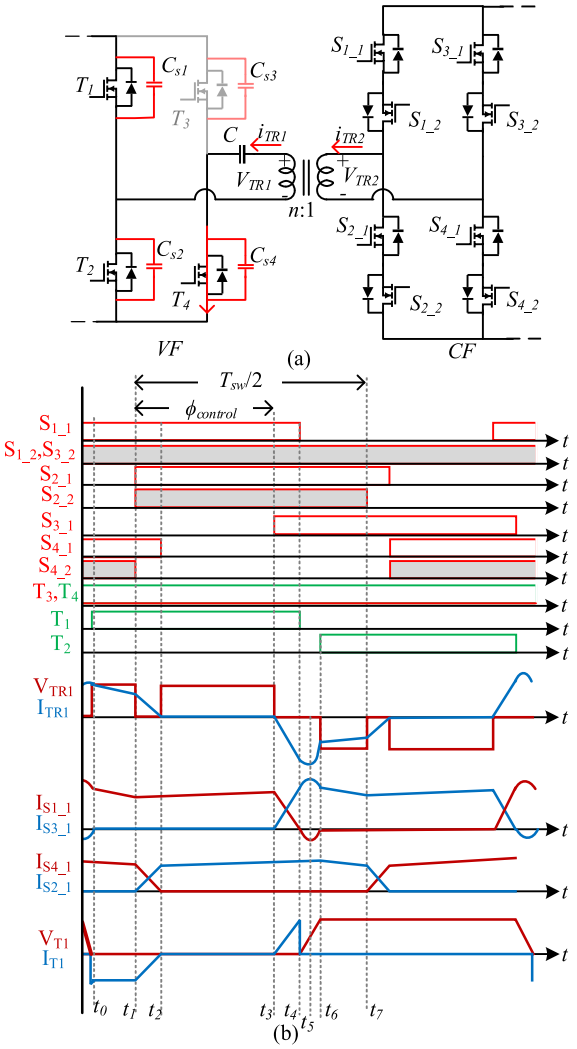

FIGURE 5. Operation of the dc-dc cell with the TMC-VF modulation (a) and the corresponding idealized voltage and current waveforms (b).

which can be written as (6).

$$G_{dc-dc} = \frac{2\pi n}{1 - \frac{\varphi_{control}}{\pi} - 2f_{sw}\left(\frac{2nL(2I_{c(max)} - I_c)}{V_{DC}} + t_{res}\right)} \tag{6}$$

C. MODULATION WITH CF-SIDE TMC (TMC-CF)

The equivalent circuit corresponding to the TMC-CF modulation is illustrated in Fig. 6 (a). The bottom switches of the CF side S_{2_1}, S_{2_2}, and S_{4_1}, S_{4_2} are modulated complementary with a duty cycle of slightly over 0.5. The VF-side switches $T_1 \ldots T_4$ are modulated in diagonals complementary with a duty cycle of slightly below 0.5.

The TMC-CF modulation is shown in Fig. 6 (b) for one switching period. During t_0- t_1, the switch S_{2_1} turns on with ZCS with the help of the leakage inductor. The interval t_2- t_3 allows the switch S_{4_1} to turn off with ZCS. In the interval t_3- t_4, the VF-switches T_1, T_4 start to turn off with ZVS assisted by the snubber capacitors C_{s1} and C_{s4}, respectively. At the same time, the snubber capacitors C_{s2} and C_{s4}

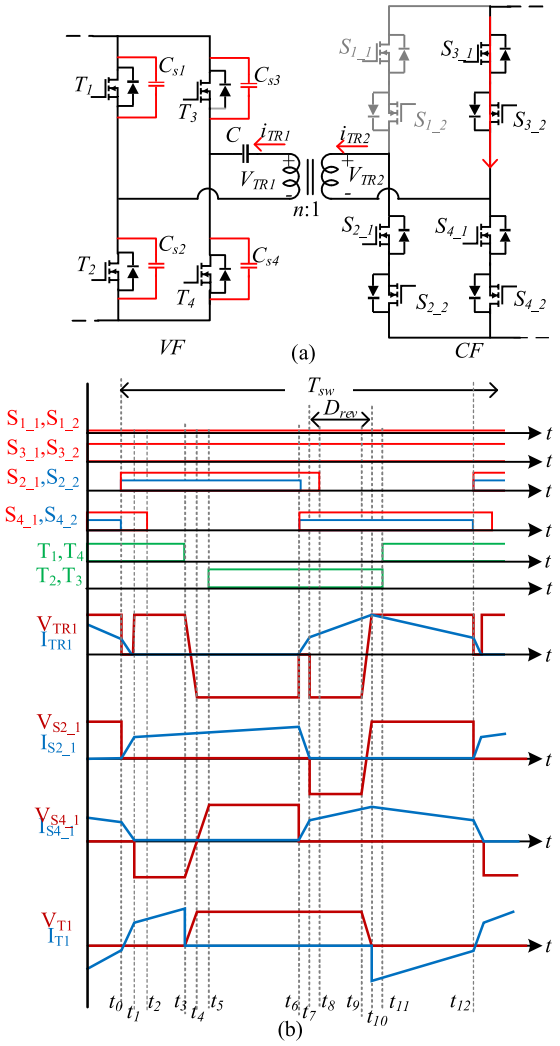

FIGURE 6. Operation of the dc-dc cell with the TMC-CF modulation (a) and the corresponding idealized voltage and current waveforms (b).

discharge to zero. The energy is delivered to the VF side during the time interval t_5-t_6 after the switches T_2 and T_3 are turned on with ZVS. Next, in the interval t_6- t_7, the CF-side switches S_{4_1} and S_{4_2} turn on with ZCS. The interval t_7- t_8 is equivalent to t_1- t_2, and it begins the reverse energy transfer direction. Interval t_8- t_9 allows S_{4_1} to turn off with ZCS. In the following intervals, i.e., t_9- t_{10} and t_{10}- t_{11}, the energy transfers from CF to VF via the transformer with the help of body diodes of T_2 and T_3, similar to the classical forward dc-dc converter. In the last interval t_{11}- t_{12}, switches T_2 and T_3 are turned on with ZVS. Therefore, the relative duration of the reverse energy transfer period (D_{rev}) is the control variable defining the dc-dc converter gain, as given in (7) from [35].

$$G_{dc-dc} = \frac{V_C}{V_{DC}} = \frac{2n}{1 - 4D_{rev}} \tag{7}$$

This modulation TMC technique was first proposed in [35]. This modulation differs from the previous two, featuring minimized energy circulation between the VF and CF sides. The TMC-CF modulation harnesses high circulating energy for charging the inductor L. As a result, the current stress factors of components would increase, but it would provide good controllability at very low voltage V_C values. Unlike the other two modulations, the TMC-CF has two voltage-boosting mechanisms: short-circuiting the inductor L and circulating the energy, where the second one is dominant.

D. SUMMARY OF THE TMC MODULATIONS

Equations (5) – (8) show that the TMC-VF and -CF modulations provide doubled dc-dc converter gain compared to the baseline modulation. These modulations could be used in the V_C range of ±60 V in the given applications.

The TMC-VF modulation reduces transformer core losses due to the twice-reduced swing of the voltage v_{TR1}, i.e., its flux density is twice lower. On the other hand, the transistors T_1 and T_2 should operate with doubled current stress. Hence, efficiency improvement is expected to be more prominent at higher dc microgrid voltages, closer to 380 V. The TMC-CF cannot reduce core losses but features fewer CF-side devices conducting current even with higher current stress.

Based on their characteristics, it could be predicted that the TMC-VF should provide higher efficiency than the TMC-CF. The following section provides experimental evaluation and benchmarking of these modulations. It is worth emphasizing that all three modulations feature soft-switching of the semiconductor devices, but the TMC-CF modulation uses circulating energy, causing higher current stress on the components.

IV. EXPERIMENTAL VERIFICATION

This section provides an extensive experimental study detailing the performance of all modulations and corresponding control variables using an experimental prototype described in the first subsection. Moreover, a discussion on performance enhancement of the case study step-up/down PPC is provided with quantification of efficiency differences.

A. PROTOTYPE DESCRIPTION

An experimental prototype (Fig. 7) was constructed. The isolation transformer was designed with a turns ratio of 2.1, according to (8). This value leaves a sufficient margin for the overlap of CF-side gating signals needed for soft-switching.

$$n \leq \frac{min\,(V_{DC})}{max\,(V_C)} = \frac{320}{130} \approx 2.46 \tag{8}$$

The transformer was designed using two parallel EE42/21/20 cores of N87 material. The windings utilize 10 turns of 2000 × 0.04 mm Litz wire and 21 turns of 1200×0.04 mm Litz wire, which results in the maximum flux density of 100 mT. This design achieves leakage and magnetizing inductance values reflected to the CF-side winding of 0.6 μH and 800 μH, respectively. The input inductor L is built using a gapped ETD54/28/19 core of 3C97 material. The dc blocking capacitor in the winding *TR1* and the capacitor in the CF port are both equal to 60 μF.

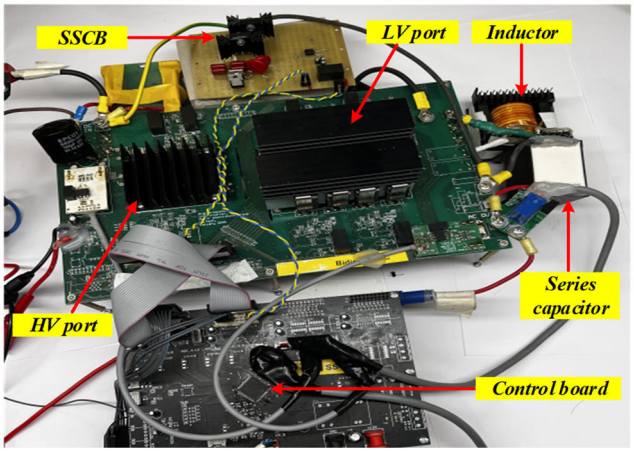

FIGURE 7. Photo of the experimental prototype.

TABLE 2. Components and parameters of the experimental prototype.

Component/Parameter	Symbol	Value/Type
LV port switches	$S_{1.1}$-$S_{4.2}$	C3M0120090D
HV port switches	T_1-T_4	C3M0120090J
Isolated gate drivers	-	UCC21520-Q1
LV port inductor	L	100µH
Inductor core	-	ETD54/28/19/3C97
Transformer leakage inductance	L_{eq}	850nH
Transformer turns ratio	n	2.3:1
Transformer core	-	ETD54/28/19/3C97
HV port capacitors	C_1=C_2	60µF (Foil)
Series capacitor	C	100µF (Foil)
HV port snubber capacitors	C_s	1.1nF (Ceramic)

To ensure robust operation during testing, 120 mΩ/900 V SiC MOSFETs were used on the VF and CF side. Despite the relatively high $R_{DS,on}$ the prototype is still viable as the converter exhibits predominantly conduction losses. Their reduction will be more prominent with this design, allowing efficiency measurement with higher accuracy. The SSCB utilizes 30 mΩ Si switches, which put the associated conduction losses below 7 W during tests. The control system is based on STM32G474 microcontrollers comprising a multichannel high-resolution PWM timer (HRTIM). The main components and parameters of the prototype are listed in Table 2.

The efficiency was measured at PV currents of 3 A, 7 A, and 10 A using a Yokogawa W1800E power analyzer with basic power accuracy of 0.05%. A bidirectional power supply from iTECH IT6000C series was used to emulate a stiff dc microgrid, while a PV string emulator Chroma 62150H-1000S was utilized as the input power source. Voltage waveforms were measured using a differential voltage probe with 100 MHz bandwidth, and the current waveforms were measured using an isolated AC/DC current probe with 120 MHz bandwidth. The probes were used with a 4-channel oscilloscope with 350 MHz bandwidth/channel.

B. PERFORMANCE EVALUATION OF THE PPC WITH BASELINE MODULATION

First, the prototype was tested without TMC modulation techniques to assess general performance trends. The measurements of the PPC and dc-dc converter efficiencies were performed for the three dc microgrid voltages: $V_{DC} = 320$ V (Fig. 8), $V_{DC} = 350$ V (Fig. 9), and $V_{DC} = 380$ V (Fig. 10). The general efficiency trade-off is that converter performance is better at lower current in the voltage step-up mode, and higher current in the step-down mode. This is caused by higher (static) circulating energy when the dc-dc converter transfers energy from the CF to the VF side [34].

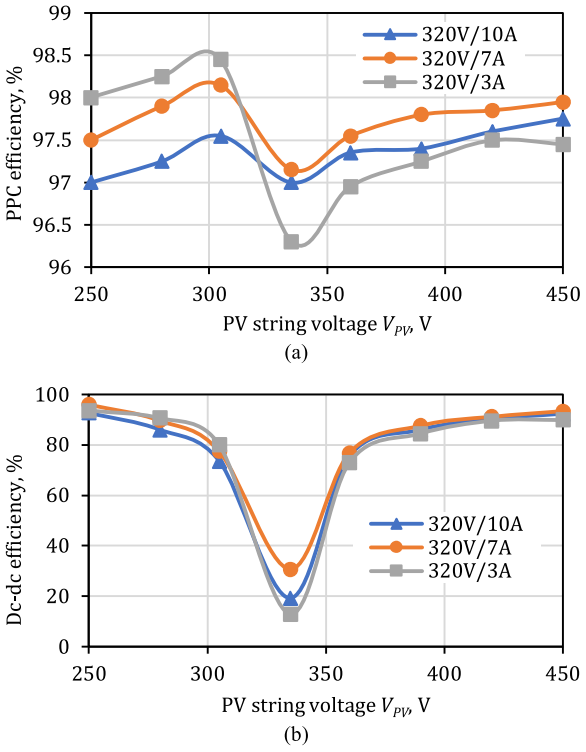

FIGURE 8. Efficiency measured with the baseline modulation at $V_{DC} = 320$ V at three current values across the PV string voltage range: (a) PPC and (b) dc-dc efficiency.

The dc-dc converter features minimum efficiency when PV string and dc microgrid voltages are equal, as could be expected from nearly zero processed power, as follows from Fig. 11. In this point, it operates with a phase shift angle of close to zero, as depicted in Fig. 12. The phase shift angle defines the dc gain, but have little dependence on the system power, only minor adjustment is needed to compensate for the increased conduction losses if the power rises. It linearly depends on the PV string voltage, while its sign defines the power transfer direction. This linearity would simplify the design of a control system, as it allows a typical PI controller to provide stable regulation.

The power processed by the dc-dc converter varies from nearly 0 W to almost 1500 W, while the PV string power

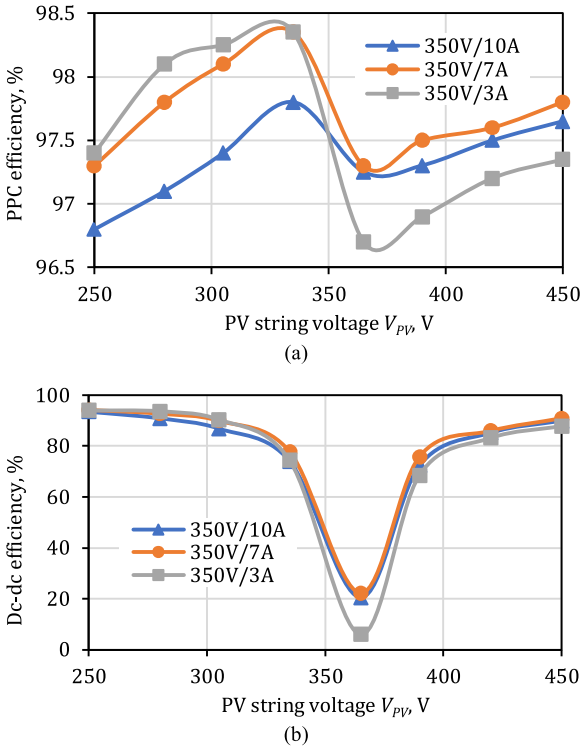

FIGURE 9. Efficiency measured with the baseline modulation at $V_{DC} = 350$ V at three current values across the PV string voltage range: (a) PPC and (b) dc-dc efficiency.

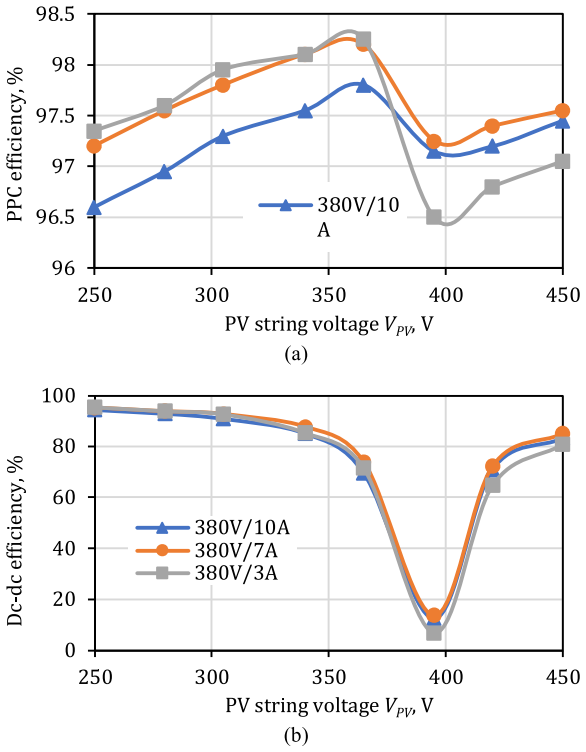

FIGURE 10. Efficiency measured with the baseline modulation at $V_{DC} = 380$ V at three current values across the PV string voltage range: (a) PPC and (b) dc-dc efficiency.

reaches up to 4.5 kW. The efficiency of dc-dc cell varies significantly, which, however, results only in a small drop in the PPC efficiency. Also, it is important to mention that

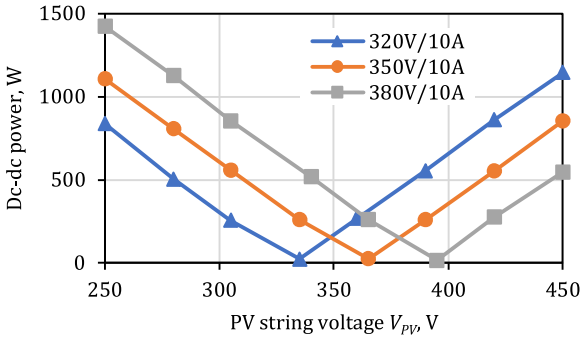

FIGURE 11. Experimentally measured active power processed by dc-dc converter plotted for three dc microgrid voltages across the PV string voltage range.

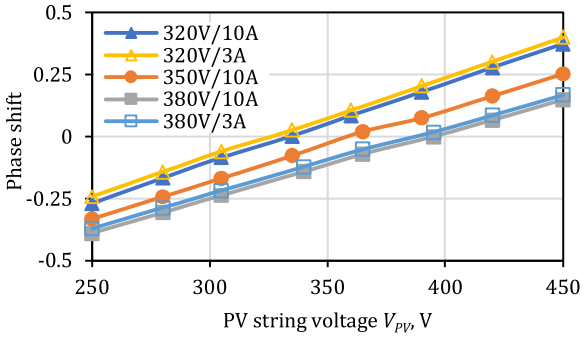

FIGURE 12. Experimental phase shift angle of the baseline modulation plotted in p.u. for five test conditions across the PV string voltage range.

the point of zero processed power is shifted from the $V_{PV} = V_{DC}$ condition due to voltage drop on the CF-side and SSCB transistors, wiring, and other ohmic losses in the converter. The dc-dc call must produce a small voltage to compensate for these resistances when the $V_{PV} = V_{DC}$.

C. PERFORMANCE EVALUATION OF THE PPC WITH TMC-VF MODULATION

The measurements of the PPC and dc-dc converter efficiencies were performed with the TMC-VF modulation for the three dc microgrid voltages: $V_{DC} = 320$ V (Fig. 13), $V_{DC} = 350$ V (Fig. 14), and $V_{DC} = 380$ V (Fig. 15). The general efficiency trade-off is similar to the baseline modulation at higher currents due to their similarity. The efficiency improved at low currents, where RMS current stress is low, and a reduction in transformer losses is more evident. The efficiency improvement over the baseline modulation could be observed. This results from the dc-dc cell operating in more favorable conditions, allowing higher overall efficiency and a smaller drop in efficiency ner zero partiality. On the other hand, it was found that current regulation near zero partiality is limited and could restrict PPC applicability.

The phase shift angle provides twice higher dc-dc gain with the TMC-VF modulation than the baseline modulation, as observed from Eqs. (5) and (6). This trend is confirmed experimentally, as can be observed in Fig. 16. As was

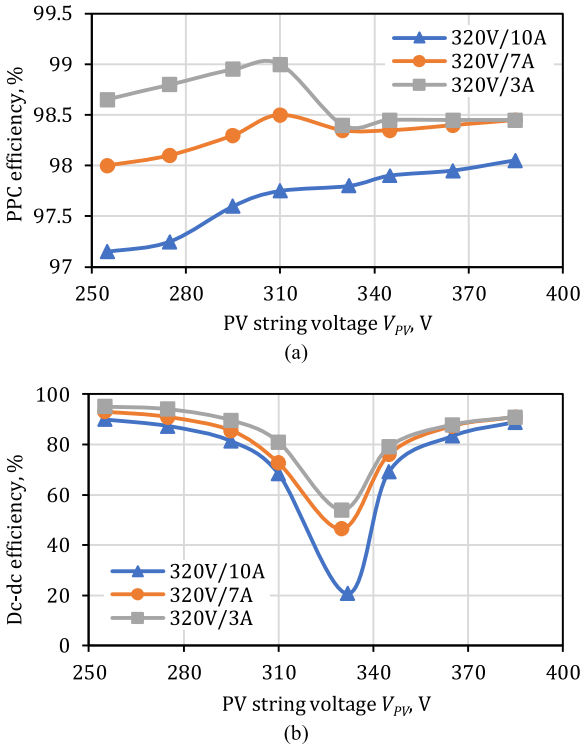

FIGURE 13. Efficiency measured with the TMC-VF modulation at V_{DC} = 320 V at three current values across the PV string voltage range: (a) PPC and (b) dc-dc efficiency.

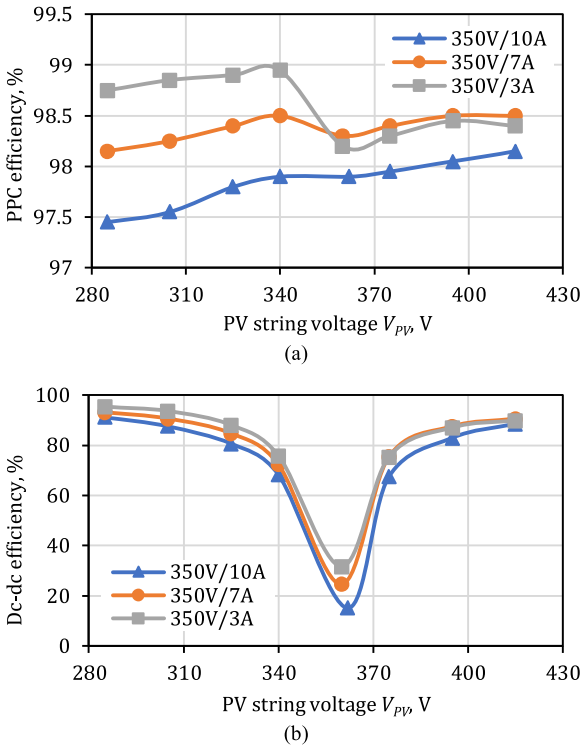

FIGURE 14. Efficiency measured with the TMC-VF modulation at V_{DC} = 350 V at three current values across the PV string voltage range: (a) PPC and (b) dc-dc efficiency.

mentioned, this modulation is feasible in the voltage range of the series port V_C, i.e., the difference between the PV string and dc microgrid voltages of ±60 V.

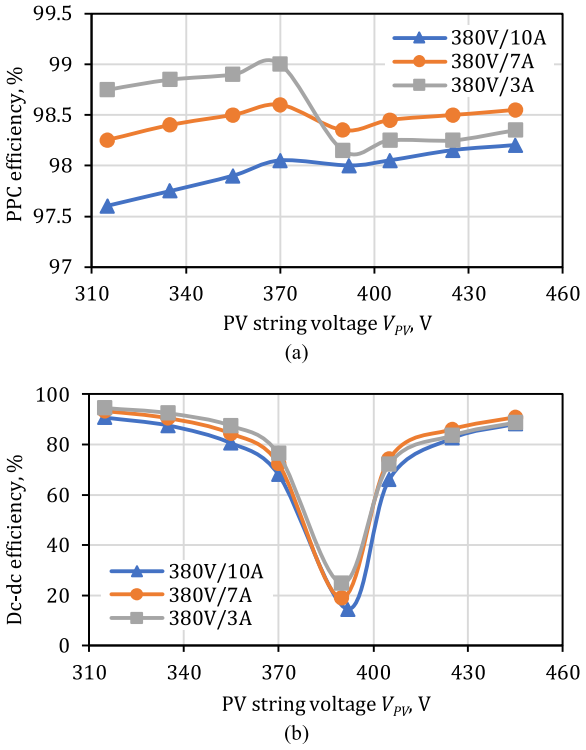

FIGURE 15. Efficiency measured with the TMC-VF modulation at V_{DC} = 380 V at three current values across the PV string voltage range: (a) PPC and (b) dc-dc efficiency.

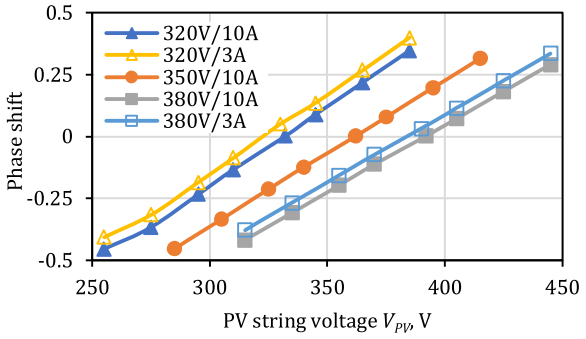

FIGURE 16. Experimental phase shift angle of the TMC-VF modulation plotted in p.u. for five test conditions across the PV string voltage range.

D. PERFORMANCE EVALUATION OF THE PPC WITH TMC-CF MODULATION

The TMC-CF modulation was also experimentally verified at three dc microgrid voltages: V_{DC} = 320 V (Fig. 17), V_{DC} = 350 V (Fig. 18), and V_{DC} = 380 V (Fig. 19). Generally, the efficiency rises when the PV string voltage increases. It follows the RMS current stress trend, defined mainly by the circulating energy. The efficiency is significantly lower in the step-up mode of the PPC due to energy transfer from the VF to the CF side. Compared to the baseline modulation, the efficiency is lower as this modulation employs a significant amount of circulating energy for current regulation. On the

other hand, this energy enables smooth current regulation near zero partiality.

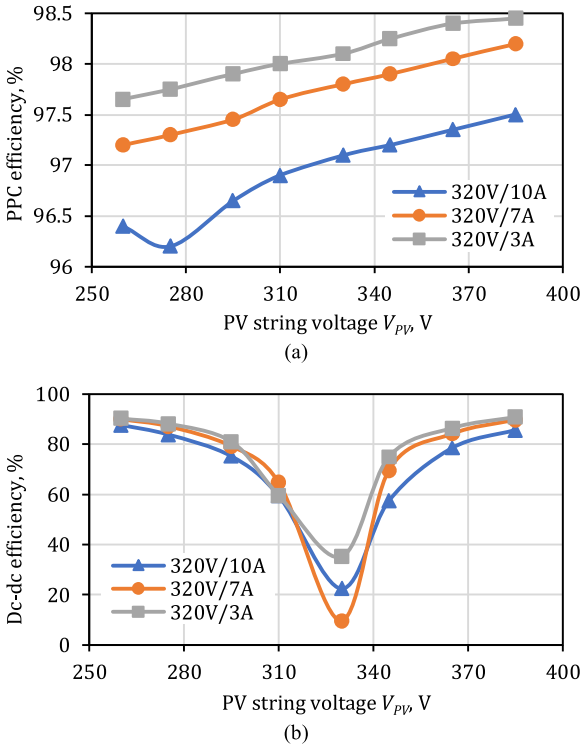

FIGURE 17. Efficiency measured with the TMC-CF modulation at V_{DC} = 320 V at three current values across the PV string voltage range: (a) PPC and (b) dc-dc efficiency.

To achieve this power flow direction, the circulating energy should be dominant. The duty cycle of the corresponding time interval, the main control variable in this mode, must be over 0.25. As a result of the reverse energy transfer from the VF to the CF side using the circulating energy, the RMS current of components increases significantly. In the step-down mode, the duty cycle of the reverse energy interval is below 0.25. As a result, the efficiency is higher. The correlation between the power loss and the reverse energy interval duration could be easily established by correlating its values from Fig. 20 and the measured efficiency curves from Figs. 17, 18, and 19. Despite the drawback of high conduction losses, this modulation features smooth behavior of the PPC efficiency curves. Also, it harnesses the circulating energy for current regulation near zero voltage at the series port. Similar to the TMC-VF modulation, the TMC-CF modulation could be applied only in the range of V_C between –60 V and +60 V.

E. COMPARISON OF MODULATION TECHNIQUES

First, to demonstrate fundamental differences between the studied modulation techniques, the experimental waveforms of the CF side current of the dc-dc converter, transformer current, and voltages across the transformer windings are shown in Figs. 21, 22, and 23 for the baseline, TMC-VF, and TMC-CF modulations, respectively. It is evident that the latter differs from the first two modulations by its operating principle and, consequently, its current/voltage waveforms.

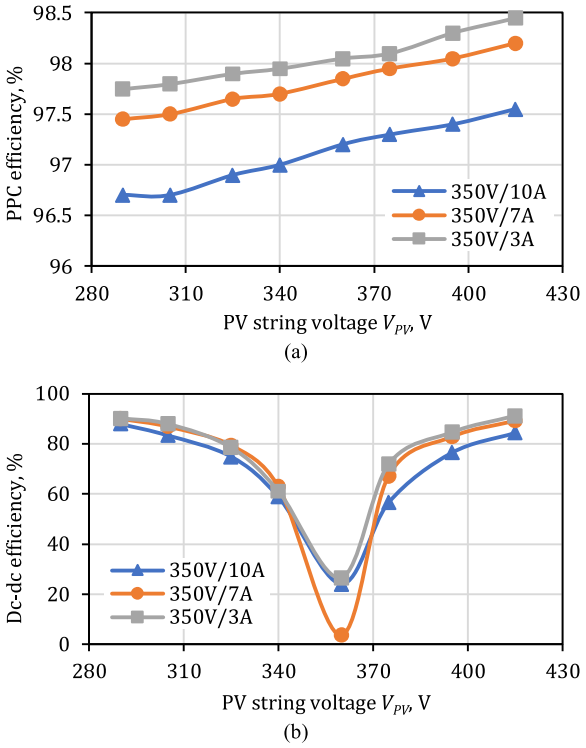

FIGURE 18. Efficiency measured with the TMC-CF modulation at V_{DC} = 350 V at three current values across the PV string voltage range: (a) PPC and (b) dc-dc efficiency.

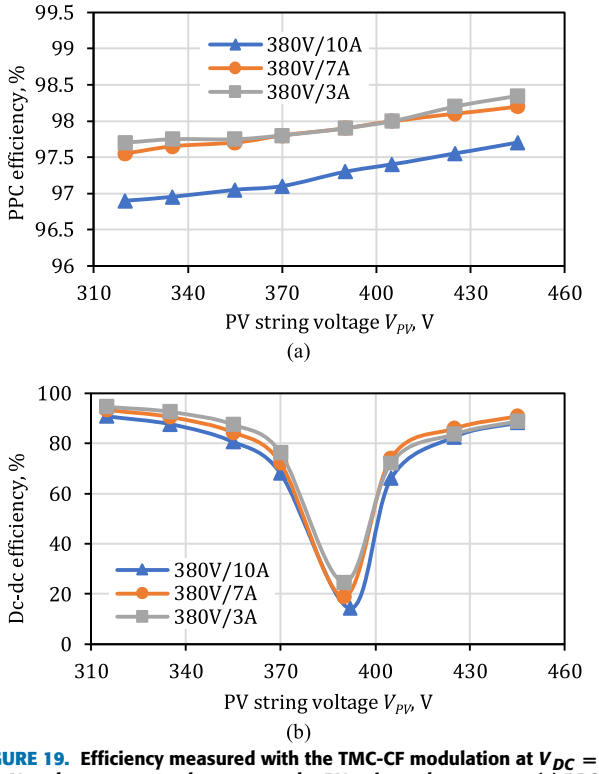

FIGURE 19. Efficiency measured with the TMC-CF modulation at V_{DC} = 380 V at three current values across the PV string voltage range: (a) PPC and (b) dc-dc efficiency.

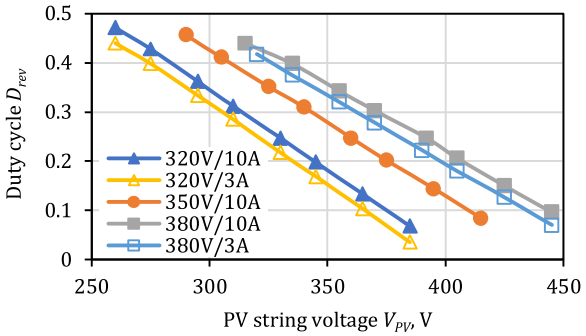

FIGURE 20. Experimental t_{REV} duty cycle of the TMC-CF modulation plotted for five test conditions across the PV string voltage range.

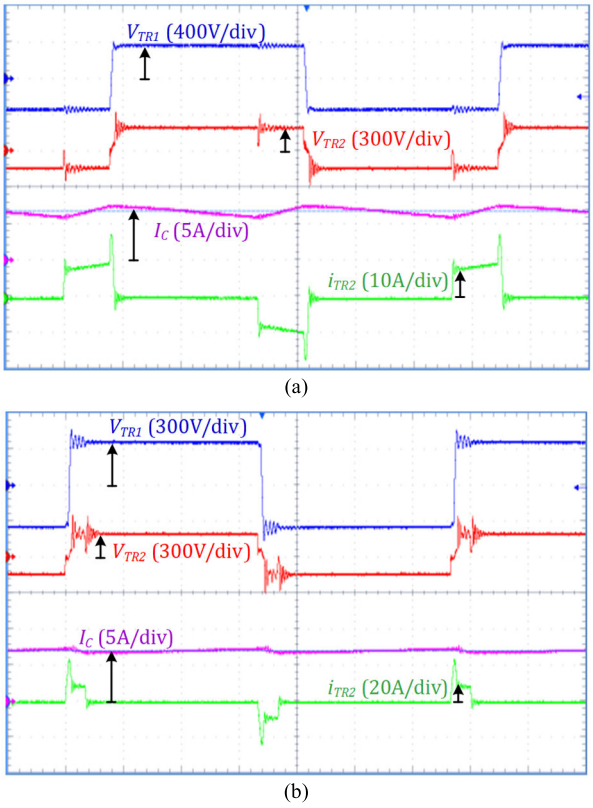

FIGURE 21. Experimental waveforms measured with the baseline modulation at the nominal dc microgrid voltage $V_{DC} = 350$ V and PV current of 7 A in (a) the step-up mode at $V_{PV} = 330$ V and (b) the step-down mode at $V_{PV} = 370$ V.

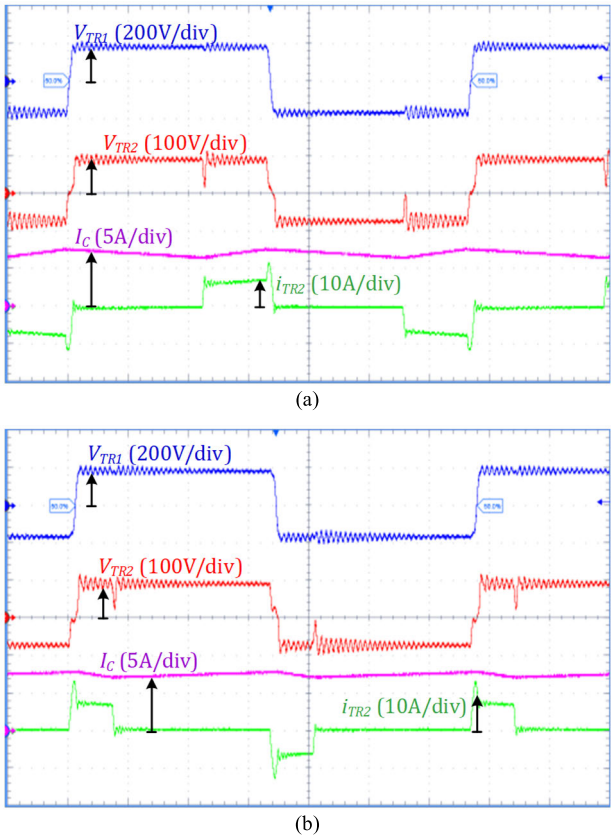

FIGURE 22. Experimental waveforms measured with the TMC-VF modulation at the nominal dc microgrid voltage $V_{DC} = 350$ V and PV current of 7 A in (a) the step-up mode at $V_{PV} = 330$ V and (b) the step-down mode at $V_{PV} = 370$ V.

First, the most obvious difference is in the swing of the voltage v_{TR2} between the baseline and TMC-VF modulations. As expected, the reduced voltage swing of the TMC-VF modulation causes, consequently, lower losses in the transformer core but higher losses in the transformer windings due to their higher RMS current. The baseline modulation features a high peak current in the transformer during the resonant soft-switching of the VF-side transistors, resulting from the higher voltage swing applied to the transformer winding. This phenomenon causes low efficiency of the baseline modulation at low loads.

The forward (from the CF to the VF side) and reverse energy transfer processes are clearly visible in the case of the TMC-CF modulation in Fig. 23. The reverse energy transfer interval is longer in the step-up mode and shorter in the step-down mode. This circulating energy results in high conduction losses in the components. Moreover, the effective operating frequency of the inductor L is equal to the switching frequency, which is twice as low as that of the other two modulations. This is caused by inductor charging only once a period, which happens at a much higher current slope resulting from the energy transfer from the VF to the CF side. As a result, the TMC-CF features a significant current ripple in the inductor L, which imposes a risk of high ac losses in the inductor windings.

The three modulations considered in this study could be compared in the V_C region of ± 60 V. Values of the efficiency difference between the TMC modulations and the baseline modulation are quantified in Fig. 24. TMC-VF always provides some increase in the PPC efficiency, which is more prominent in the step-down mode. In the step-down mode, the RMS currents are lower, which assists this increase in efficiency. In general, it features an efficiency trend similar to that of the baseline modulation. Considering their close

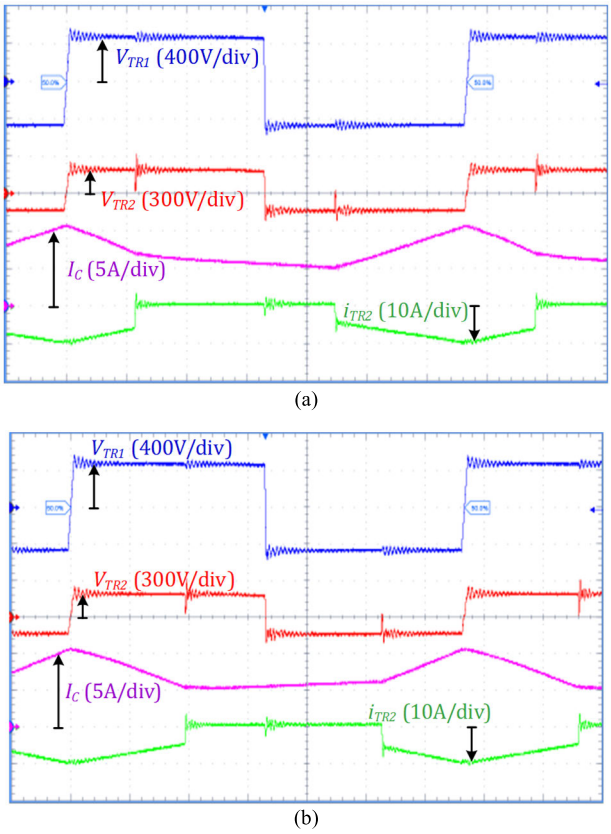

FIGURE 23. Experimental waveforms measured with the TMC-CF modulation at the nominal dc microgrid voltage $V_{DC} = 350$ V and PV current of 7 A in (a) the step-up mode at $V_{PV} = 330$ V and (b) the step-down mode at $V_{PV} = 370$ V.

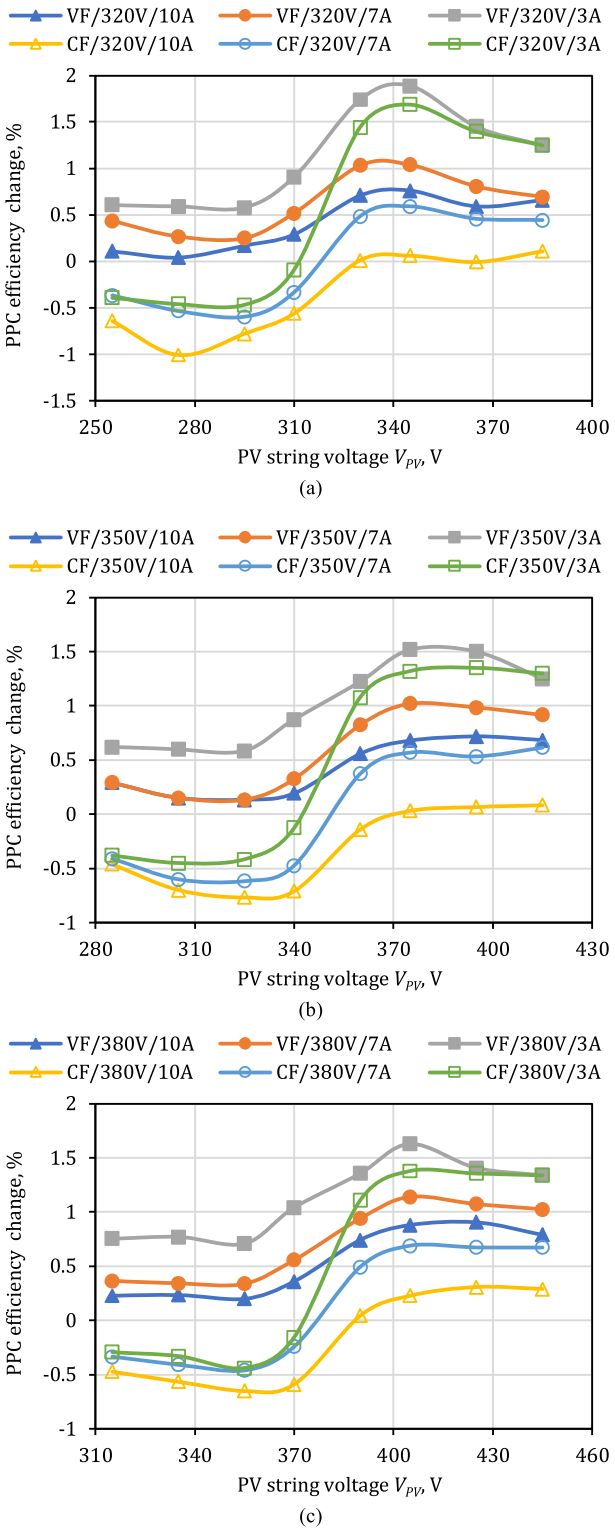

FIGURE 24. Experimental efficiency difference caused by the application of the TMC in the FV and the CF sides measured for three PV currents (3 A, 7 A, and 10 A) at three voltages of the dc microgrid: (a) 320 V, (b) 350 V, and (c) 380 V.

relations, both baseline and TMC-VF modulations demonstrate very similar voltage/current waveforms.

As expected, the TMC-CF modulation performs worse than the TMC-VF. It causes up to 1% of PPC efficiency drop in the step-up mode due to high circulating energy levels. This issue is diminished in the step-down mode, resulting in up to 1.7% efficiency improvement. Nevertheless, its performance regarding PPC efficiency is worse than TMC-VF can provide. Hence, the TMC-CF should be avoided in applications where efficiency is paramount. However, it will find its applications where high regulation performance near zero voltage at the series PPC port is required, even at the expense of a small drop in efficiency. Such an application could be a drooped-controlled battery energy storage, where small voltage variations cause sizable current variations.

Maximum power point tracking (MPPT) was implemented to demonstrate the benefits of TMC-CF modulation in terms of voltage regulation, as shown in Fig. 25 (a). In practice, the converter pre-charges the series capacitance to the maximum voltage difference and then initiates MPPT operation, as shown in Fig. 25 (b). A solar array simulator, Chroma 62150H-1000S, implemented synthetic tests with rapid changes in equivalent PV cell temperature (*Temp*) to achieve fast changes in the maximum power point voltage of a PV string at around 350 V. TMC-CF modulation enables MPPT with a smooth transition through the zero partiality

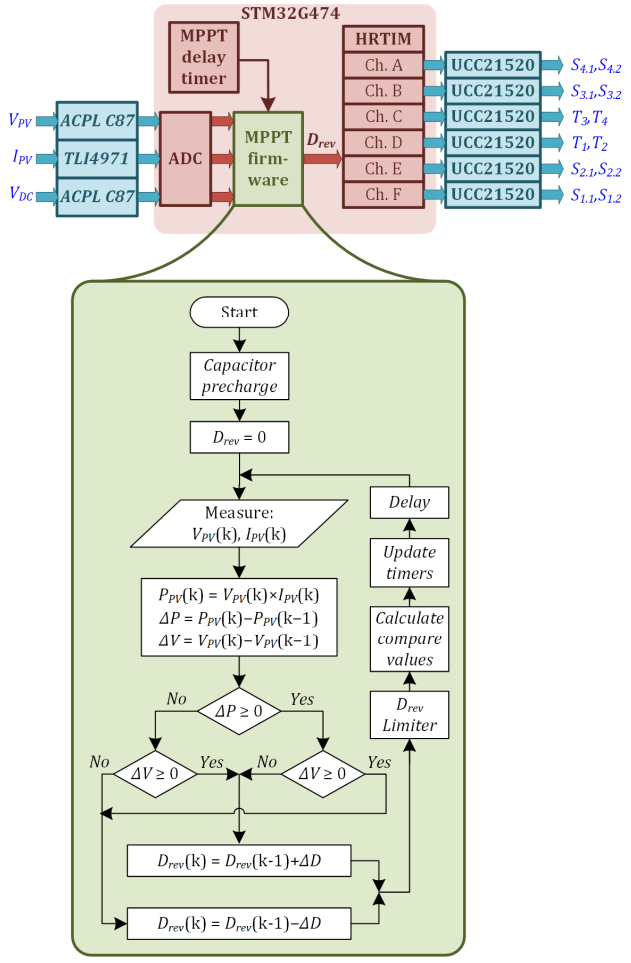

(a)

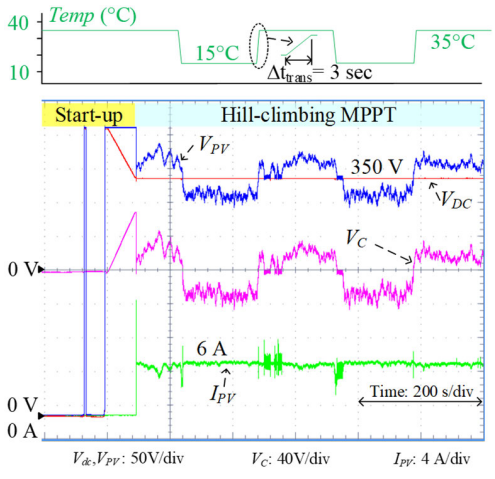

(b)

FIGURE 25. PPC operation with TMC-CF modulation: (a) implementation of the hill-climbing MPPT, and (b) PPC start-up and MPPT routine.

region, providing MPPT efficiency of roughly 99%. Six channels of high-resolution timer HRTIM was used for TMC-CF implementation, while generic embedded times defined the delay between MPPT perturbations. Used MOSFET drivers and current/voltage sensors are also indicated in the figure.

V. CONCLUSION

This study provides a comprehensive modeling of possible PV string configurations composed of 54-, 60-, and 66-cell PV modules, considering both hot and cold climates. It shows that a wide selection of available residential PV modules allows for restricting the PV string voltage range from 250 V to 450 V. At least 14 PV string configurations could fit this MPP voltage window. They range from 3 kW to 6 kW, covering the majority of residential rooftop installations. Combining this voltage range with the droop-control voltage range of ±30 V used in typical residential dc microgrids makes it possible to draw application requirements for partial power interface converters for PV string integrations in dc microgrids. Such an analysis has not been performed before. It yields that step-up/down PPC should be capable of operating in the ±130 V range of the series port and rated for 1.6 kW to cover the majority of residential rooftop PV string use cases. Such a PPC can perform best if its parallel port is connected to a dc microgrid.

A PPC was prototyped according to the derived application requirements. It achieves a peak efficiency of 99%. Nevertheless, its overall efficiency across the studied operating conditions is limited due to operating with relatively high partiality, i.e., the share of the active power processed by the isolated dc-dc cell. Recent research shows that topology morphing control can improve the performance of galvanically isolated dc-dc converters. It was proposed that PPCs could also benefit from this technique.

The applicability of the topology morphing control in PPCs was demonstrated in this study for the first time. Two topology morphing control techniques have been proposed to enhance the PPC efficiency in the ±60 V range of the series port voltage. The efficiency of the given PPC was improved by up to 1.9%. The case-study topology features soft switching of all semiconductor components, and efficiency improvement is associated with reduced conduction power losses.

Other PPC topologies and configurations should be studied regarding their feasibility according to the synthesized application requirements and applicability of the topology morphing control.

REFERENCES

[1] K. Hainsch, K. Löffler, T. Burandt, H. Auer, P. C. del Granado, P. Pisciella, and S. Zwickl-Bernhard, "Energy transition scenarios: What policies, societal attitudes, and technology developments will realize the EU green deal?" *Energy*, vol. 239, Jan. 2022, Art. no. 122067.

[2] M. Wei, C. A. Mcmillan, and S. de la Rue du Can, "Electrification of industry: Potential, challenges and outlook," *Current Sustain./Renew. Energy Rep.*, vol. 6, no. 4, pp. 140–148, Nov. 2019.

[3] Z. Tang, Y. Yang, and F. Blaabjerg, "Power electronics: The enabling technology for renewable energy integration," *CSEE J. Power Energy Syst.*, vol. 8, no. 1, pp. 39–52, Jan. 2022.

[4] D. Tan, "Emerging system applications and technological trends in power electronics: Power electronics is increasingly cutting across traditional boundaries," *IEEE Power Electron. Mag.*, vol. 2, no. 2, pp. 38–47, Jun. 2015.

[5] J. F. Martins, E. Romero-Cadaval, D. Vinnikov, and M. Malinowski, "Transactive energy: Power electronics challenges," *IEEE Power Electron. Mag.*, vol. 9, no. 1, pp. 20–32, Mar. 2022.

[6] I. Kougias, N. Taylor, G. Kakoulaki, and A. Jäger-Waldau, "The role of photovoltaics for the European green deal and the recovery plan," *Renew. Sustain. Energy Rev.*, vol. 144, Jul. 2021, Art. no. 111017.

[7] B. Hallam, M. Kim, R. Underwood, S. Drury, L. Wang, and P. Dias, "A polysilicon learning curve and the material requirements for broad electrification with photovoltaics by 2050," *Sol. RRL*, vol. 6, no. 10, pp. 1–12, Aug. 2022.

[8] I. Verbytskyi, M. Lukianov, K. Nassereddine, B. Pakhaliuk, O. Husev, and R. M. Strzelecki, "Power converter solutions for industrial PV applications—A review," *Energies*, vol. 15, no. 9, p. 3295, Apr. 2022.

[9] I. Vairavasundaram, V. Varadarajan, P. J. Pavankumar, R. K. Kanagavel, L. Ravi, and S. Vairavasundaram, "A review on small power rating PV inverter topologies and smart PV inverters," *Electronics*, vol. 10, no. 11, p. 1296, May 2021.

[10] E. Pikas, J. Kurnitski, M. Thalfeldt, and L. Koskela, "Cost-benefit analysis of nZEB energy efficiency strategies with on-site photovoltaic generation," *Energy*, vol. 128, pp. 291–301, Jun. 2017.

[11] G. Cillari, A. Franco, and F. Fantozzi, "Sizing strategies of photovoltaic systems in nZEB schemes to maximize the self-consumption share," *Energy Rep.*, vol. 7, pp. 6769–6785, Nov. 2021.

[12] D. Kolantla, S. Mikkili, S. R. Pendem, and A. A. Desai, "Critical review on various inverter topologies for PV system architectures," *IET Renew. Power Gener.*, vol. 14, no. 17, pp. 3418–3438, Dec. 2020.

[13] S. Pantano, R. Heard, and R. E. Brown, "DC appliances and DC power distribution: A bridge to the future net zero energy homes," Lawrence Berkeley Nat. Lab., Berkeley, CA, USA, Tech. Rep. LBNL-2001084, Sep. 2017.

[14] T. Castillo-Calzadilla, M. A. Cuesta, C. Olivares-Rodriguez, A. M. Macarulla, J. Legarda, and C. E. Borges, "Is it feasible a massive deployment of low voltage direct current microgrids renewable-based? A technical and social sight," *Renew. Sustain. Energy Rev.*, vol. 161, Jun. 2022, Art. no. 112198.

[15] V. Vossos, D. L. Gerber, M. Gaillet-Tournier, B. Nordman, R. Brown, W. B. Heredia, O. Ghatpande, A. Saha, G. Arnold, and S. M. Frank, "Adoption pathways for DC power distribution in buildings," *Energies*, vol. 15, no. 3, p. 786, Jan. 2022.

[16] O. Abdel-Rahim, A. Chub, D. Vinnikov, and A. Blinov, "DC integration of residential photovoltaic systems: A survey," *IEEE Access*, vol. 10, pp. 66974–66991, 2022.

[17] N. G. F. dos Santos, J. R. R. Zientarski, and M. L. S. Martins, "A review of series-connected partial power converters for DC–DC applications," *IEEE J. Emerg. Sel. Topics Power Electron.*, vol. 10, no. 6, pp. 7825–7838, Dec. 2022.

[18] J. R. R. Zientarski, M. L. da Silva Martins, J. R. Pinheiro, and H. L. Hey, "Evaluation of power processing in series-connected partial-power converters," *IEEE J. Emerg. Sel. Topics Power Electron.*, vol. 7, no. 1, pp. 343–352, Mar. 2019.

[19] M. S. Agamy, M. Harfman-Todorovic, A. Elasser, S. Chi, R. L. Steigerwald, J. A. Sabate, A. J. McCann, L. Zhang, and F. J. Mueller, "An efficient partial power processing DC/DC converter for distributed PV architectures," *IEEE Trans. Power Electron.*, vol. 29, no. 2, pp. 674–686, Feb. 2014.

[20] J. W. Zapata, S. Kouro, G. Carrasco, H. Renaudineau, and T. A. Meynard, "Analysis of partial power DC–DC converters for two-stage photovoltaic systems," *IEEE J. Emerg. Sel. Topics Power Electron.*, vol. 7, no. 1, pp. 591–603, Mar. 2019.

[21] O. Abdel-Rahim, A. Chub, H. M. Maheri, A. Blinov, and D. Vinnikov, "High-performance buck-boost partial power quasi-Z-source series resonance converter," *IEEE Access*, vol. 10, pp. 130177–130189, 2022.

[22] C. Liu, Z. Zhang, and M. A. E. Andersen, "Analysis and evaluation of 99% efficient step-up/down converter based on partial power processing," *IEEE Trans. Ind. Electron.*, early access, Aug. 17, 2022, doi: 10.1109/TIE.2022.3198241.

[23] J. R. R. Zientarski, M. L. d. S. Martins, J. R. Pinheiro, and H. L. Hey, "Series-connected partial-power converters applied to PV systems: A design approach based on step-up/down voltage regulation range," *IEEE Trans. Power Electron.*, vol. 33, no. 9, pp. 7622–7633, Sep. 2018.

[24] J. Anzola, I. Aizpuru, A. A. Romero, A. A. Loiti, R. Lopez-Erauskin, J. S. Artal-Sevil, and C. Bernal, "Review of architectures based on partial power processing for DC–DC applications," *IEEE Access*, vol. 8, pp. 103405–103418, 2020.

[25] V. Sidorov, A. Chub, D. Vinnikov, and F. Z. Peng, "Survey of topology morphing control techniques for performance enhancement of galvanically isolated DC–DC converters," *IEEE Open J. Ind. Electron. Soc.*, vol. 3, pp. 751–777, 2022.

[26] E. L. Carvalho, A. Blinov, A. Chub, P. Emiliani, G. de Carne, and D. Vinnikov, "Grid integration of DC buildings: Standards, requirements and power converter topologies," *IEEE Open J. Power Electron.*, vol. 3, pp. 798–823, 2022.

[27] T. Jalakas, R. Kosenko, A. Chub, D. Vinnikov, and A. Blinov, "Current-fed partial power converter for photovoltaic applications in DC microgrids," in *Proc. 47th Annu. Conf. IEEE Ind. Electron. Soc.*, Toronto, ON, Canada, Oct. 2021, pp. 1–5.

[28] Qcell. *Q.PEAK DUO BLK M-G11 SERIES*. Accessed: Nov. 7, 2023. [Online]. Available: https://media.qcells.com/v/9FW78hNP/

[29] Trina Solar. *The ResidentialModule Multi-Busbar Mono PERC Module. Model: TSM-DE06X.05(II)*. Accessed: Nov. 7, 2023. [Online]. Available: https://static.trinasolar.com/sites/default/files/Datasheet_DE06X.05%28II%29_NA_2021_A.pdf

[30] Canadian Solar. *HiKuBlack All-Black High Power Mono Perc Module*. Accessed: Nov. 7, 2023. [Online]. Available: https://static.csisolar.com/wp-content/uploads/2019/12/10125855/CS-Datasheet-HiKuBlack_CS3L-MS_v5.8_EN-12y.pdf

[31] A. Chub, K. Roman, O. Korkh, D. Vinnikov, and S. Kouro, "Energy yield assessment methodology for photovoltaic microinverters," in *Proc. IEEE 15th Brazilian Power Electron. Conf. 5th IEEE Southern Power Electron. Conf. (COBEP/SPEC)*, Santos, Brazil, Dec. 2019, pp. 1–5.

[32] N. Hassanpour, A. Chub, A. Blinov, and D. Vinnikov, "Soft switching bidirectional step-Up/Down partial power converter with reduced components stress," *IEEE Trans. Power Electron.*, vol. 38, no. 11, pp. 14166–14177, Nov. 2023.

[33] A. Blinov, R. Kosenko, D. Vinnikov, and L. Parsa, "Bidirectional isolated current-source DAB converter with extended ZVS/ZCS range and reduced energy circulation for storage applications," *IEEE Trans. Ind. Electron.*, vol. 67, no. 12, pp. 10552–10563, Dec. 2020.

[34] A. Blinov, D. Vinnikov, E. Romero-Cadaval, J. Martins, and D. Peftitsis, "Isolated high-frequency link PFC rectifier with high step-down factor and reduced energy circulation," *IEEE J. Emerg. Sel. Topics Ind. Electron.*, vol. 3, no. 3, pp. 788–796, Jul. 2022.

[35] A. Blinov, R. Kosenko, A. Chub, and V. Ivakhno, "Analysis of fault-tolerant operation capabilities of an isolated bidirectional current-source DC–DC converter," *Energies*, vol. 12, no. 16, p. 3203, Aug. 2019.

ANDRII CHUB (Senior Member, IEEE) received the B.Sc. and M.Sc. degrees in electronic systems from Chernihiv State Technological University, Ukraine, in 2008 and 2009, respectively, and the Ph.D. degree in electrical engineering from the Tallinn University of Technology, Tallinn, Estonia, in 2016.

He was a Visiting Research Fellow with Kiel University, in 2017, and a Postdoctoral Researcher with Federico Santa Maria Technical University, from 2018 to 2019. He is currently a Senior Researcher with the Power Electronics Group, Department of Electrical Power Engineering and Mechatronics, Tallinn University of Technology. He has coauthored over 200 articles and several book chapters on power electronics and applications and holds several patents and utility models. His research interests include advanced dc–dc converter topologies, renewable energy conversion systems, energy-efficient buildings, reliability, and fault-tolerance of power electronic converters.

Dr. Chub is the Chair of the Joint IES/PELS/IAS/PES Chapter of the IEEE Estonia Section. He is an Associate Editor of IEEE JOURNAL OF EMERGING AND SELECTED TOPICS IN INDUSTRIAL ELECTRONICS.

NASER HASSANPOUR (Student Member, IEEE) received the B.Sc. and M.Sc. degrees in electrical engineering from the University of Tabriz, Iran, in 2012 and 2016, respectively. He is currently pursuing the Ph.D. degree with the Department of Electrical Power Engineering and Mechatronics, Tallinn University of Technology, Tallinn, Estonia.

His work mainly focuses on dc–dc converters for residential applications.

NEELESH YADAV (Member, IEEE) received the dual B.Tech. and M.Tech. degrees from Lovely Professional University, Punjab, India, in 2016, and the Ph.D. degree from the Indian Institute of Technology Mandi, Kamand, India, in 2022.

He is currently a Postdoctoral Researcher with the Power Electronics Group, Tallinn University of Technology, Estonia. His research interests include control and power management in dc microgrids, fault detection, and ac–dc/dc–dc power electronic converters.

TANEL JALAKAS (Member, IEEE) received the Ph.D. degree in electrical engineering from the Tallinn University of Technology (TalTech), Estonia, in 2010.

He is currently a Senior Researcher with the Department of Electrical Power Engineering and Mechatronics, TalTech. He has coauthored over 80 publications. His main research interest includes the design of power electronic converters for renewable energy sources.

ANDREI BLINOV (Senior Member, IEEE) received the M.Sc. and Ph.D. degrees in electrical drives and power electronics from the Tallinn University of Technology, Tallinn, Estonia, in 2008 and 2012, respectively. His Ph.D. dissertation devoted to the research of switching properties and performance improvement methods of high-voltage IGBT-based dc–dc converters.

After the Ph.D. studies, he has spent two years in Sweden as a Postdoctoral Researcher with the KTH Royal Institute of Technology. He is currently a Senior Researcher with the Department of Electrical Power Engineering and Mechatronics, Tallinn University of Technology. He has over 100 publications in the areas related to power electronics and holds several patents and utility models. He was involved in organization of IEEE conferences, special sessions, and workshops in the areas related to electric vehicle charging and battery storage. His research interests include switch-mode power converters, new semiconductor technologies, renewable energy, and battery storage systems.

DMITRI VINNIKOV (Fellow, IEEE) received the Dipl.Eng., M.Sc., and Dr.Sc.Techn. degrees in electrical engineering from the Tallinn University of Technology, Tallinn, Estonia, in 1999, 2001, and 2005, respectively.

He is currently the Head of the Power Electronics Group, Department of Electrical Power Engineering and Mechatronics, Tallinn University of Technology. He is also the Head of Research and Development and the Co-Founder of Ubik Solutions LLC—an Estonian start-up company dedicated to innovative and smart power electronics for renewable energy systems. Moreover, he is one of the founders and leading researchers of ZEBE–Estonian Centre of Excellence for zero energy and resource-efficient smart buildings and districts. He has authored or coauthored two books, five monographs, and one book chapter, as well as more than 400 published articles on power converter design and development, and is the holder of numerous patents and utility models in this field. His research interests include the applied design of power electronic converters and control systems, renewable energy conversion systems (photovoltaic and wind), impedance-source power converters, and the implementation of wide bandgap power semiconductors.

Dr. Vinnikov is the Chair of the IEEE Estonia Section.